

On the shape and completeness of the column density probability distribution function of molecular clouds

Bastian Körtgen^{1*}, Christoph Federrath² and Robi Banerjee¹

¹ *Hamburger Sternwarte, Universität Hamburg, Gojenbergsweg 112, 21029 Hamburg, Germany*

² *Research School of Astronomy and Astrophysics, Australian National University, Canberra, ACT 2611, Australia*

Released 2018

ABSTRACT

Both observational and theoretical research over the past decade has demonstrated that the probability distribution function (PDF) of the gas density in turbulent molecular clouds is a key ingredient for understanding star formation. It has recently been argued that the PDF of molecular clouds is a pure power-law distribution. It has been claimed that the log-normal part is ruled out when using only the part of the PDF up/down to which it is complete, that is where the column density contours are still closed. By using the results from high-resolution magnetohydrodynamical simulations of molecular cloud formation and evolution, we find that the column density PDF is indeed composed of a log-normal and, if including self-gravity, a power-law part. We show that insufficient sampling of a molecular cloud results in closed contours that cut off the log-normal part. In contrast, systematically increasing the field of view and sampling the entire cloud yields a completeness limit at the lower column densities, which also recovers the log-normal part. This demonstrates that the field of view must be sufficiently large for the PDF to be complete down to its log-normal part, which has important implications for predictions of star-formation activity based on the PDF.

Key words: methods: numerical, (magnetohydrodynamics) MHD, turbulence, stars: formation, ISM: clouds, ISM: kinematics and dynamics

1 INTRODUCTION

The (column-) density probability distribution function (henceforth N-PDF or PDF) has become a powerful tool to analyse the dynamics of molecular clouds both from an observational (Elmegreen & Scalo 2004; Kainulainen et al. 2009; Brunt 2010; Ginsburg et al. 2013; Kainulainen et al. 2013; Lombardi et al. 2014; Burkhart et al. 2015; Schneider et al. 2015, 2016; Federrath et al. 2016) and a theoretical perspective (Passot & Vázquez-Semadeni 1998; Federrath et al. 2008, 2010; Konstandin et al. 2012; Girichidis et al. 2014; Nolan et al. 2015; Federrath & Banerjee 2015; Burkhart et al. 2017). For isothermal gas, its shape is best described by a log-normal function as a consequence of interacting turbulent shocks modifying the density structure (Vázquez-Semadeni 1994). Mathematically, this shape can be understood from the central-limit theorem of an ensemble of independent events (Passot & Vázquez-Semadeni 1998; Kritsuk et al. 2007; Federrath et al. 2010). In contrast, in a thermally unstable gas, a multiphase medium is formed, which consequently results in a multi-peaked PDF, with the peaks being

located at the characteristic density of each phase (Pikel’Ner 1968; Field et al. 1969; Gazol et al. 2001, 2005). However, the clear separation of the different peaks might become washed out, when the turbulent motions in the unstable gas become sufficiently strong (Vázquez-Semadeni et al. 2000; Audit & Hennebelle 2005).

The high-density fraction of the PDF has either a log-normal shape for isothermal, non-self-gravitating gas or forms a power-law tail, when the dense gas structures are dominated by gravity (Federrath & Klessen 2013; Kainulainen et al. 2014; Girichidis et al. 2014) or have an equation of state softer than isothermal (i.e. $\gamma < 1$). A physical explanation for the emergence of a power-law tail due to gravity was given by Kritsuk et al. (2011). The authors showed that the formation of power-law density profiles in (small-scale) gravitationally collapsing regions naturally leads to a power-law in the density PDF and thus also in the N-PDF (see also Federrath & Klessen 2013, and references therein). In contrast, Lombardi et al. (2015) suggest that the power-law form of the PDF arises because the entire molecular cloud can be described by a power-law density profile.

But, there can also be other reasons for a power-law tail. It was shown that gas compression by external pressure (Trem-

* bkoertgen@hs.uni-hamburg.de

blin et al. 2014) or sufficiently strong turbulence in the thermally bistable gas can also yield a power-law tail (Vázquez-Semadeni et al. 2000). Ballesteros-Paredes et al. (2011) have studied the evolution of the N-PDF of a molecular cloud formed in numerical simulations of a thermally unstable gas including self-gravity. They showed that a power-law tail naturally develops when self-gravity becomes important, but that the double-peak signature arising from thermal instability is still visible in the PDF. With these previous studies in mind, there might indeed arise a PDF, where the signature of thermal instability is blurred and which thus shows a power-law tail all the way down to the lowest densities.

The information content of the N-PDF is biased by several effects, such as by contamination from clouds lying in the fore- or background (Lombardi et al. 2015; Schneider et al. 2015; Ossenkopf-Okada et al. 2016). As discussed in Schneider et al. (2015) and Ossenkopf-Okada et al. (2016), this can be corrected for by subtraction of a constant offset. However, as Schneider et al. (2015) point out, such an approach might over- or underestimate the influence of the line-of-sight contamination. In addition, Lombardi et al. (2015) and Ossenkopf-Okada et al. (2016) show that it is mainly the low-density part of the PDF that is affected by the contamination, whereas the high-density (power-law) part is nearly unaffected.

However, it has recently been argued that N-PDFs, after subtraction of an offset to correct for contamination, are no longer log-normal, but rather show only a power-law form (Lombardi et al. 2015). A theoretical approach was conducted by Ward et al. (2014), who study N-PDFs in synthetic observations of simulated molecular clouds. The authors showed that dynamically old clouds show a log-normal part in combination with a power-law tail, but that the log-normal part systematically falls below the visual extinction threshold. Ward et al. (2014) conclude that a pure power-law distribution might thus be due only to limited observational resolution.

The retrieved information of a PDF is only reliable within its completeness limit (Kainulainen et al. 2013). From an observational perspective, it has been suggested that the PDF is complete down to the smallest column density with a closed contour (Kainulainen et al. 2013). By using this definition, it has recently been argued that column density PDFs of a variety of high galactic latitude clouds (diffuse or star-forming) have a power-law shape when the last closed contour defines the completeness of the PDF (Alves et al. 2017). These authors stated that there is no observational evidence for log-normal PDFs and that molecular clouds have PDFs well described by power laws.

In this study, we analyse the N-PDF of molecular clouds formed in three-dimensional, magnetohydrodynamical simulations of converging flows. We estimate the value of the *last closed contour* as a function of a varying field of view for a star-forming and a quiescent region within the formed cloud complex, as well as for the entire complex and study the obtained N-PDF. We show that the value of the last closed contour moves towards higher column densities for a decreasing field of view. We find that the log-normal part of the N-PDF is well within the completeness of the PDF for a sufficiently large field of view, emphasising that N-PDFs are indeed composed of a log-normal part (and a power-law tail, when gravitational collapse sets in).

This paper is organised as follows: In section 2 we introduce the numerical setup and the initial conditions. Section 3 provides a brief description of the general time evolution of the formed clouds and a comparison of the resulting N-PDF for a case with and without self-gravity but otherwise identical parameters. This is followed by the presentation of our results of the N-PDF for different extents of the fields of view of two molecular cloud regions in section 4, and our conclusions are given in section 5.

2 SIMULATION DATA AND METHODS

The simulations presented here were carried out with the FLASH code in version 2.5 (Fryxell et al. 2000).

We set up two cylindrical flows of warm neutral medium (WNM) gas with a length $l = 112 \text{ pc}$ and a radius of $R = 64 \text{ pc}$, which collide head-on in the centre of the cubic simulation domain, which has a volume of $V_{\text{sim}} = (256 \text{ pc})^3$. The computational domain is initially filled with gas of number density $n = 1 \text{ cm}^{-3}$ and temperature $T = 5000 \text{ K}$. The gas is able to heat and cool via optically-thin radiation, which is given in tabulated form according to the prescription by Koyama & Inutsuka (2002) and used as a source term in the energy equation. The fitting functions for the heating and cooling rates are given by

$$\Gamma = 2 \times 10^{-26} \text{ ergs}^{-1}, \quad (1)$$

with the heating rate Γ , and

$$\frac{\Lambda(T)}{\Gamma} = 10^7 \exp\left(\frac{-1.184 \times 10^5}{T + 1000}\right) + 1.4 \times 10^{-2} \sqrt{T} \exp\left(\frac{-92}{T}\right), \quad (2)$$

where $\Lambda(T)$ is the temperature-dependent cooling rate and T the temperature in Kelvin (Koyama & Inutsuka 2002; Vázquez-Semadeni et al. 2007). By using this definition, the gas is initially in the thermally unstable regime and will develop into a two-phase medium.

The sound speed at the initial temperature is $c_s = 5.7 \text{ km s}^{-1}$ and the WNM flows are initialised with a flow velocity of $v_F = 11.4 \text{ km s}^{-1}$, which corresponds to a isothermal Mach number of $\mathcal{M}_F = 2$, being thus mildly supersonic. In order to trigger dynamical and thermal instabilities, the flows are additionally turbulent with $\mathcal{M}_{\text{RMS}} = 1$, and the energy spectrum is of Burgers type, $E(k) \propto k^{-2}$ (Ossenkopf & Mac Low 2002; Heyer & Brunt 2004).

Since the interstellar medium of galaxies is also magnetised (Crutcher et al. 2010; Beck 2012), we add a magnetic field $\mathbf{B} = B_0 \hat{\mathbf{x}}$ aligned parallel to the flows with $\hat{\mathbf{x}}$ being the unit vector in the x-direction. The initial magnitude is $B_0 = 3 \mu\text{G}$ in all simulations, indicating that the flows are magnetically critical with a normalised mass-to-magnetic flux ratio of $\mu/\mu_{\text{crit}} \sim 1$. Note that accretion of gas from the environment will rapidly increase the mass-to-flux ratio so that the cloud will be highly supercritical¹.

¹ Please note that this statement is only true for the region defined by the flow geometry. The mass-to-flux ratio of the whole box stays constant (and supercritical) due to the choice of periodic boundary conditions.

The simulations presented here use the adaptive mesh refinement technique (Berger & Olinger 1984; Berger & Colella 1989). The root grid is at resolution of $\Delta x_{\text{root}} = 64$ pc. To sufficiently resolve the dynamics at the initial stages, the collision layer is refined to a resolution of $\Delta x_{\text{layer}} = 1$ pc. We allow for a maximum of 12 refinement levels, which gives a minimum cell size of $\Delta x = 0.0156$ pc. The grid is refined once the local Jeans length is resolved with less than 8 grid cells. To prevent the gas from fragmenting artificially, we introduce Lagrangian sink particles when the gas is, besides other checks, at a density of $n_{\text{thresh}} = 3 \times 10^5 \text{ cm}^{-3}$, which represent stellar clusters rather than individual stars due to the limited spatial resolution. This ensures that the simulations are fully resolved and fragmentation of the cloud is due to physical processes (Truelove et al. 1997; Federrath et al. 2010). Feedback from sink particles via winds, radiation or supernovae is not included in the simulations, such that our simulations are probing the density PDF produced by turbulent, magnetised inflowing gas streams and gravity alone.

With these initial conditions at hand, the following set of equations of ideal magnetohydrodynamics in combination with Poisson’s equation for the self-gravity of the gas and heating and cooling is solved during each time-step

$$\begin{aligned}
 \frac{\partial}{\partial t} \varrho + \nabla \cdot (\varrho \mathbf{u}) &= 0 \\
 \varrho \frac{\partial}{\partial t} \mathbf{u} + \varrho (\mathbf{u} \cdot \nabla) \mathbf{u} &= -\nabla P_{\text{tot}} + \varrho \mathbf{g} + \frac{(\mathbf{B} \cdot \nabla) \mathbf{B}}{4\pi} \\
 \frac{\partial}{\partial t} E + \nabla \cdot \left[(E + P_{\text{tot}}) \mathbf{u} - \frac{(\mathbf{B} \cdot \mathbf{u}) \mathbf{B}}{4\pi} \right] &= \varrho \mathbf{u} \cdot \mathbf{g} + n\Gamma - n^2 \Lambda \\
 \frac{\partial}{\partial t} \mathbf{B} + \nabla \times (\mathbf{B} \times \mathbf{u}) &= 0 \\
 \nabla \cdot \mathbf{B} &= 0 \\
 \nabla^2 \Phi_{\text{gas}} &= 4\pi G \varrho.
 \end{aligned} \tag{3}$$

In the above set of equations, ϱ , \mathbf{u} and \mathbf{B} denote the gas mass density, the gas velocity and the magnetic field, respectively. The total energy density and pressure are given by $E = \varrho \epsilon_{\text{int}} + \varrho/2 |\mathbf{u}|^2 + 1/(8\pi) |\mathbf{B}|^2$ and $P_{\text{tot}} = P_{\text{th}} + 1/(8\pi) |\mathbf{B}|^2$, respectively. Furthermore, the gravitational acceleration $\mathbf{g} = -\nabla \Phi_{\text{gas}} + \mathbf{g}_{\text{sinks}}$ consists of the acceleration from the gravitational potential of the gas and the acceleration by sink particles. This set of equations is numerically solved by using the HLL5R Riemann solver to calculate the fluxes across cell boundaries (Bouchut et al. 2009; Waagan et al. 2011) and a tree-solver to calculate the gravitational potential (optimised for GPUs Lukat & Banerjee 2016). For the (magneto-)hydrodynamics we apply periodic boundary conditions, while we use isolated ones for the gravity. This choice of mixed boundary conditions is purely of numerical convenience and does not affect any of our results as we only extract and use data far away from the boundaries, i.e., where the molecular cloud forms.

An overview of the main simulation parameters is given in Table 1 and we refer the reader to Körtgen & Banerjee (2015) for a more detailed description of the initial setup.

Table 1. Summary of the main simulation parameters.

Edge length	256 pc
Min. cell size	0.015625 pc
Flow length	112 pc
Flow radius	64 pc
$\mathcal{M}_{\text{flow}}$	2
\mathcal{M}_{rms}	1
$(B_x, B_y, B_z)_{\text{init}}$	(3,0,0) μG
T_{init}	5000 K
n_{init}	1 cm^{-3}

3 RÉSUMÉ OF THE GENERAL CLOUD EVOLUTION

In this section we briefly recap the evolution of the molecular clouds formed in the shocked slab between the converging WNM streams (see e.g. Banerjee et al. 2009; Körtgen et al. 2016, 2017).

The time evolution of the cloud formed in the simulation, having an initial turbulent Mach number $\mathcal{M}_{\text{RMS}} = 1.0$, is shown in Fig. 1. The (dynamical) time for the gas at the outer edges of the flows to reach the center is $t \sim 10$ Myr, so the column density maps present the more evolved stages of the cloud. The top row of Fig. 1 shows the cloud complex face-on, where the line of sight is along the initial flow direction. The bottom row depicts an edge-on view. Generally it is seen that the cloud is composed of filaments and dense clumps, which appear at the intersection of multiple filaments. At late times, the previously tenuous regions between the filaments are seen to be denser since the cloud is collapsing globally (see also Vázquez-Semadeni et al. 2017). The turbulence generated by the inflows and by gravity shapes the morphology in the sense that the filamentary morphology prevails.

At $t = 14.5$ Myr the cloud size is comparable to the size of the flows. The edge-on view reveals a bent morphology, which is the result of dynamical instabilities that are triggered by the turbulence within the flows. Over the course of the evolution, the cloud is observed to shrink in size, due to the aforementioned collapse on a global scale. As the free-fall time is much shorter for the denser parts on smaller scales (Heitsch & Hartmann 2008; Vázquez-Semadeni et al. 2009; Hennebelle & Chabrier 2011; Federrath & Klessen 2012), hierarchical fragmentation has led to the formation of sink particles in the cloud interior. As more and more regions are collapsing the number of sink particles increases. At the last time shown, the number of sink particles has grown to $N_{\text{sink}} = 16$, where most of them are in close orbits around each other, because of further fragmentation of the parental core, so that only a handful are readily seen.

The outskirts of the cloud are observed to be highly irregular. Initially, dynamical instabilities distort the gas flows. At late times, the accretion flow onto the cloud is turbulent, which leads to further irregularity of the cloud boundaries (Klessen & Hennebelle 2010).

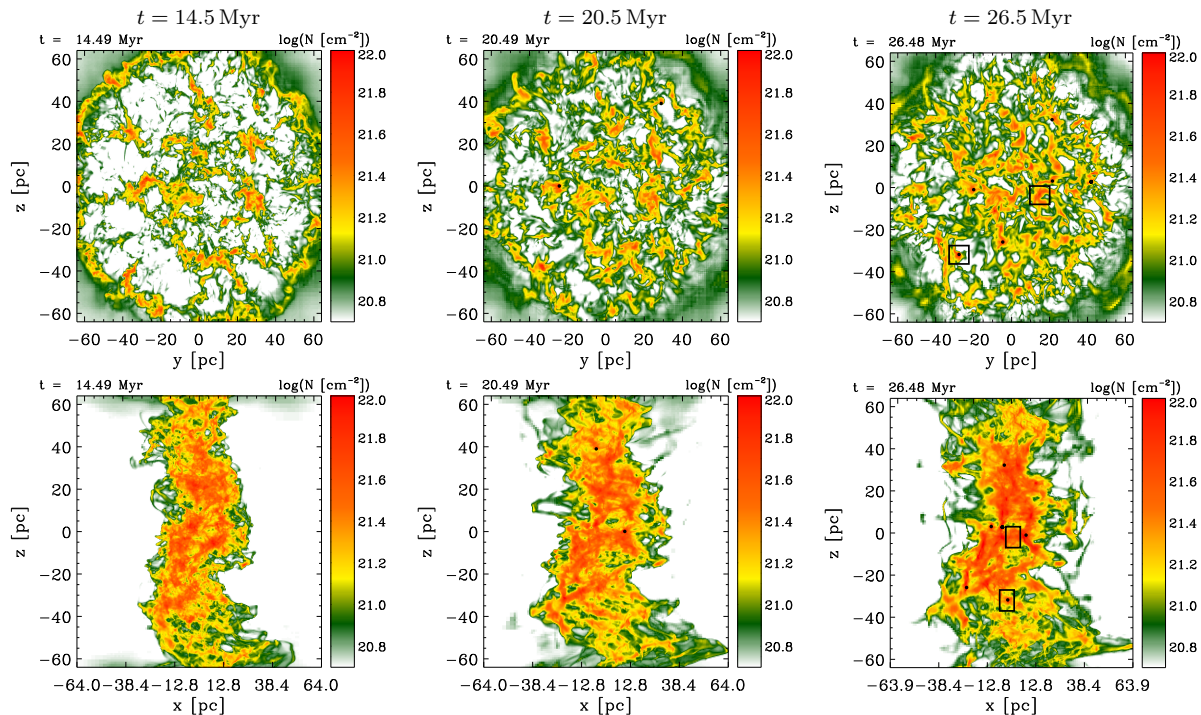


Figure 1. Column density maps of the cloud complex formed in between the WNM flows at different times (from left to right: 14.5 Myr, 20.5 Myr, and 26.5 Myr). The upper panels show the complex seen face-on, that is, along the flow direction. Bottom panels show an edge-on view. The black dots represent sink particles and the black boxes highlight the regions that will be analysed in more detail below. Integration length is $L = 160$ pc in all cases.

3.1 The shape of the column density probability distribution function

In Fig. 2 we show the column density PDF at different times and for simulations without and with self-gravity. We remind the reader that the dynamical time of the flows is $t \sim 10$ Myr. The cloud evolution shown here is thus not influenced anymore by the initially coherent inflowing gas streams from the WNM.

The PDF of the non-gravitating gas is composed of multiple peaks at $\log(N/\text{cm}^{-2}) \sim 19.6, 20.1$ and 20.7 , respectively. The leftmost peak at the lower column density is the surrounding medium. It shows a small width, because it is non-turbulent initially. The middle and right peaks show more evolution. At early times, $t = 14.5$ Myr, the peaks appear to be well separated due to the action of thermal instability and the resulting differentiation into a multiphase medium (see e.g. Iwasaki & Inutsuka 2014). However, this double-peaked signature becomes weaker at later times (see also Vázquez-Semadeni et al. 2000). It is further seen that the PDF shifts towards lower column densities. Initially, gas is being compressed by the flows and starts to expand, once the compressing agent has vanished. The high-density part of the PDF appears to be not significantly different from a log-normal at any time. We point out that, in our case, the emergence of a power-law tail is thus solely due to gravity and not due to gas thermodynamics.

In contrast, the evolution of the PDF in the case with self-gravity is different. Firstly, with time, the PDF shifts towards higher column densities (in the high-density regime) due to the influence of self-gravity. Secondly, the emergence of a power-tail is already seen (see also Ballesteros-Paredes

et al. 2011, who study the evolution of the N-PDF in a thermally bistable, gravitationally influenced medium). Furthermore, the shape of the PDF in certain column density regimes appears to vary more over time (e.g. around $\log(N/\text{cm}^{-2}) \sim 20$). For comparison, the non-self gravitating simulation shows (more or less) just a shift of the PDF, but no clear variation.

4 RESULTS

4.1 Methodology of the cloud analysis

We here present the results of our analysis on the column density PDF. In the upper right panel of Fig. 1 we highlight the studied regions and in Table 2 we provide information on the details of the analysis. We focus on two regions: The first one is star-forming. One sink particle has already formed and the column density map indicates a strongly condensed region, forming a new sink particle in the future. The second region is a quiescent one with no sink particles and slightly lower, but still comparable column density to the first one. This region furthermore shows a centrally condensed column density structure.

For the analysis, we proceed as follows: We first produce a column density map of the specific region. Next, we calculate column density contours with a contour spacing of $\Delta \log(N/\text{cm}^{-2}) = 0.01$ in square fields of view (FoV) of varying side-length centered around the center of the region and estimate the value of the *last closed* contour. This is then highlighted in the column density map and in the N-PDF of

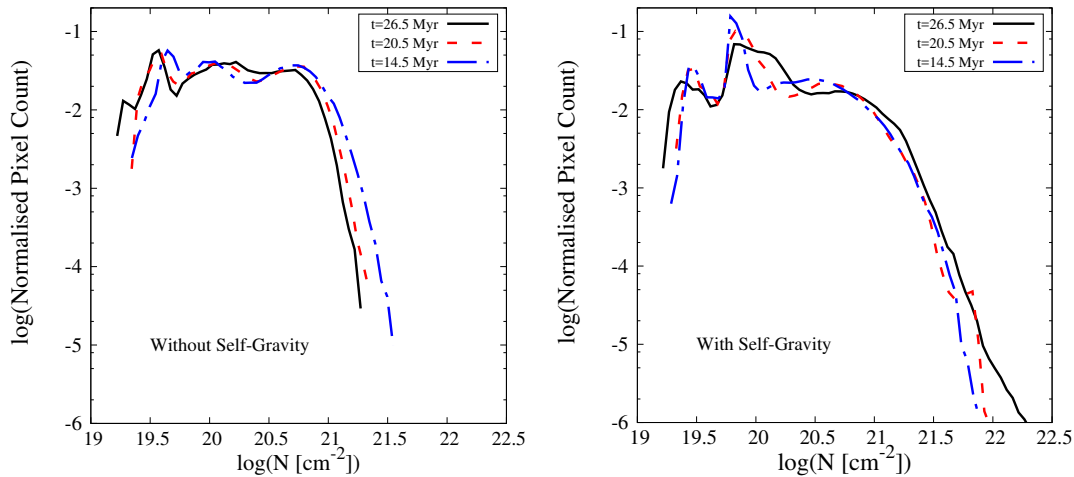


Figure 2. Column density PDF at three times for the whole cloud complex in scenarios without (left) and with self-gravity (right). Four differences are readily seen. At first, the peak of the PDF shifts to slightly higher column densities for the case with self-gravity. Secondly, due to self-gravity, higher column densities are reached. The shape of the PDF is composed of multiple peaks in the case *without* self-gravity due to the greater influence of thermal instability, whose signature appears to be washed out in the case with self-gravity. Last, in the case with self-gravity, power-law tails emerge.

Table 2. Center-position of the analysed regions and list of square boxes used for data analysis in each region.

Region	X (pc)	Y (pc)	Z (pc)
Region 1	0	-27.7	-32
Region 2	0	14.75	-3.75

Box edge length (pc)	A	B	C
Region 1	10.5	5.25	3
Region 2	16	8	4

the individual FoV.

4.2 The completeness of the N-PDF

In Fig. 3 we show column density maps of the star-forming region 1 with overlaid column density contours. Some information can be found in Tab. 2. The FoV decreases from left to right, covering areas of $10 \times 10 \text{ pc}^2$, $5 \times 5 \text{ pc}^2$ and $\sim 3 \times 3 \text{ pc}^2$. This region is composed of a centrally condensed part near the already formed sink particle, which is embedded in a larger-scale filamentary structure (see also Fig. 1). The coloured contour lines depict the last closed contour and we additionally show them within the next larger FoV. In the bottom row of the same figure, we show the column density distribution of the individual FoV. The value of the last closed contour is indicated by the coloured vertical line. It is evident that the value of the last closed contour shifts towards higher column densities, being at $\log(N/\text{cm}^{-2}) = 20.9$ for the largest and at $\log(N/\text{cm}^{-2}) = 21.6$ for the smallest FoV. Furthermore, it is evident that the distribution *above* this value changes significantly. For the smallest FoV, it resembles a power-law tail, as this area is dominated by gravity. A small change in the slope of the power-tail is also ob-

served for $\Delta \log(N/\text{cm}^{-2}) \sim 22.7$, probably being indicative of a rotationally supported structure on the smallest scales (e.g. Kritsuk et al. 2011). Increasing the field of view results in a slight shift of the value of the last closed contour to smaller column densities. Also for this FoV, the distribution above the last closed contour more closely resembles that of a power-law distribution, though the last closed contour is now seen to be closer to the turnover of the distribution. Increasing the field of view even further results in a larger shift of the last closed contour towards even smaller column densities. It is now evident that the *resolved* distribution above the closed contour *does not resemble a pure power-law distribution* anymore. This distribution also includes part of the log-normal turnover, though we emphasise that it does not completely fall within the completeness limit.

For comparison, we show in Fig. 4 the column density maps and corresponding distributions for a non-star-forming region. This region appears to be also centrally condensed, with the column density profile being rather flat near the centre. The FoV is $16 \times 16 \text{ pc}^2$, $8 \times 8 \text{ pc}^2$ and $4 \times 4 \text{ pc}^2$. We point out that, in this region, it is not clear how to interpret the shape of the column density distribution at larger column densities. However, it is still evident that the value of the last closed contour shifts towards lower column densities with increasing FoV, which shows that the above stated argument also holds for other regions within the formed cloud complex.

4.2.1 The last closed contour in a turbulent environment

So far we have studied the last closed contour for relatively centrally condensed regions. The left panel in Fig. 4 highlights the effects of a turbulent environment, in which various overdensities appear within the FoV. If these regions are of similar column density or a high column density region resides near the boundaries of the field of view, this will lead to a value of the last closed contour that is at column densities well within the power-law tail. Instead, one has to

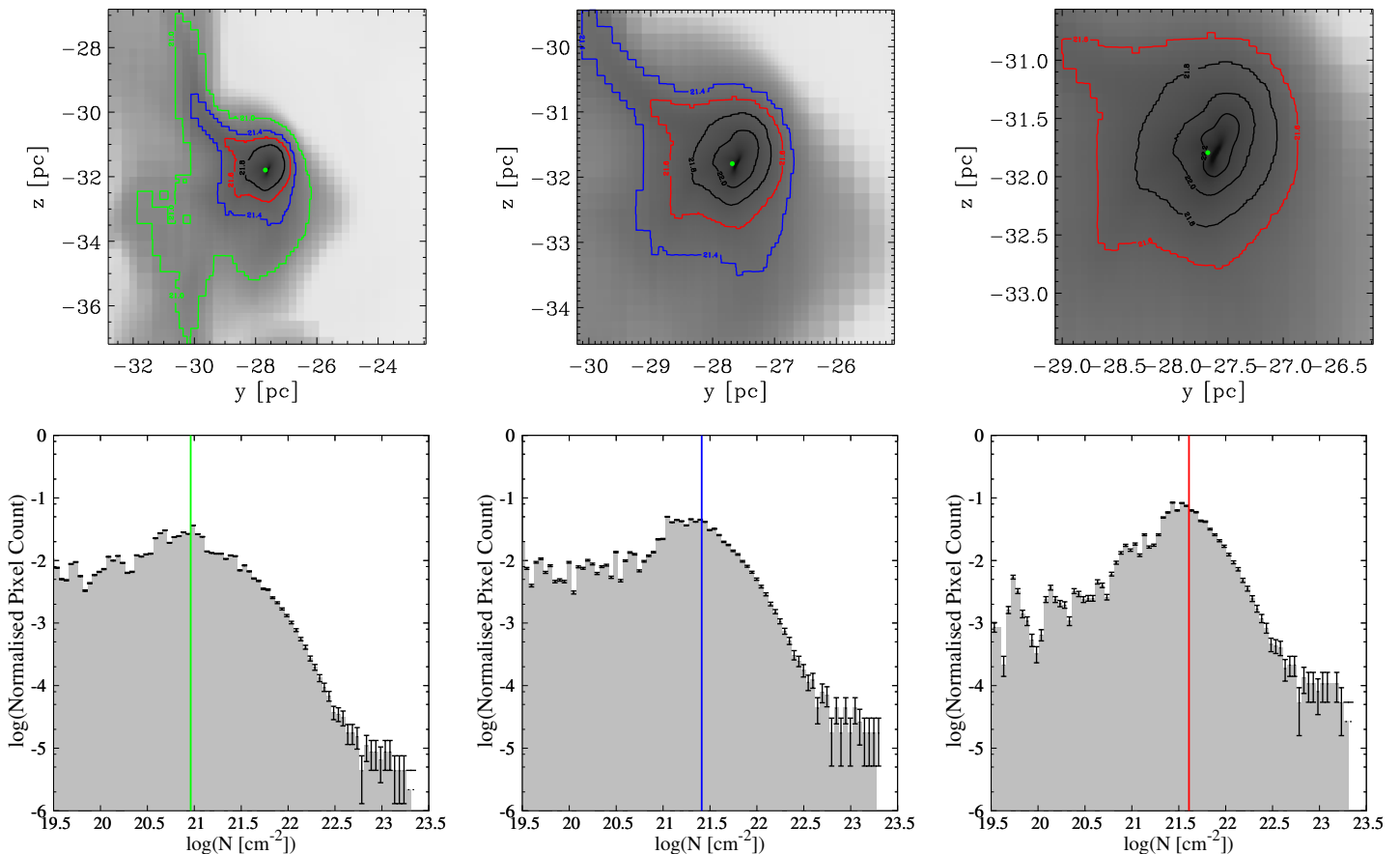


Figure 3. *Top:* Column density maps of a region undergoing gravitational collapse with decreasing field of view from $10 \times 10 \text{ pc}^2$ (left), over $5 \times 5 \text{ pc}^2$ (middle) to $3 \times 3 \text{ pc}^2$ (right). The data range is 19 (white) $< \log(N [\text{cm}^{-2}]) < 23$ (black). Overlaid are contour lines of the column density. The green, blue and red contour lines indicate the *last closed contour* for the largest, intermediate and smallest field of view, respectively. Black lines denote closed contours with contour spacing of $\Delta \log(N) = 0.2$. *Bottom:* Corresponding column density PDF (grey) with overlaid value of the last closed contour, which highlights the completeness limit. The black error bars denote the Poisson errors of each bin, calculated as $\sqrt{N_{\text{bin}}}$ with N_{bin} being the pixel count of each bin. It is clearly seen that, for a larger field of view, more and more of the PDF, which deviates from a power-law falls within the completeness limit. Note the gradual shift of the value of the last closed contour towards higher column densities for decreasing field of view.

consider that in a fully turbulent medium, there will essentially be no closed contour anymore for a sufficiently low column-density threshold. This is just natural for a turbulent medium, so the current way of using closed contours to define a column-density threshold basically excludes the log-normal peak by construction. This applies in particular for regions, where only a single last closed contour is accepted within the FoV. Such single closed contours can only be the result of gravitational collapse and hence those will only capture the very highest-density part of the PDF, where gravitational collapse has turned the high-density wing of the original log-normal PDF into a power-law tail.

Fig. 5 shows the column density distribution for a varying field of view for the whole cloud complex that has been formed in the compression layer of the two converging, turbulent WNM flows. Highlighted by vertical lines are the values of the last closed contour for the given field of view. It is obvious that, in the case of a turbulent, and thus patchy, environment, the last closed contour is well within the power-law regime of the distribution. Only the largest field of view, which captures the entire initial radial extent of the WNM flows and some diffuse gas, is able to also resolve the turnover

in the distribution. We, however, caution here that this is based on our rather idealised simulation setup and things will look differently in the real ISM.

5 CONCLUSIONS

We have presented results from molecular cloud formation simulations to study the completeness of the column density PDF. The clouds have been formed in the shocked layer between two supersonically converging streams. We have produced column density maps and PDFs of two different, but centrally condensed regions within the formed complex to study the shape and completeness of the PDF. In a next step, we calculated the value of the last closed contour in order to estimate the completeness limit of the N-PDFs. We have found qualitatively good agreement of the shape of the N-PDF with previous observational and numerical studies. We then showed that the last closed column-density contour moves towards higher column densities with decreasing size of the field of view. This means that, for too small sizes of the field of view, the N-PDF is only complete from the begin-

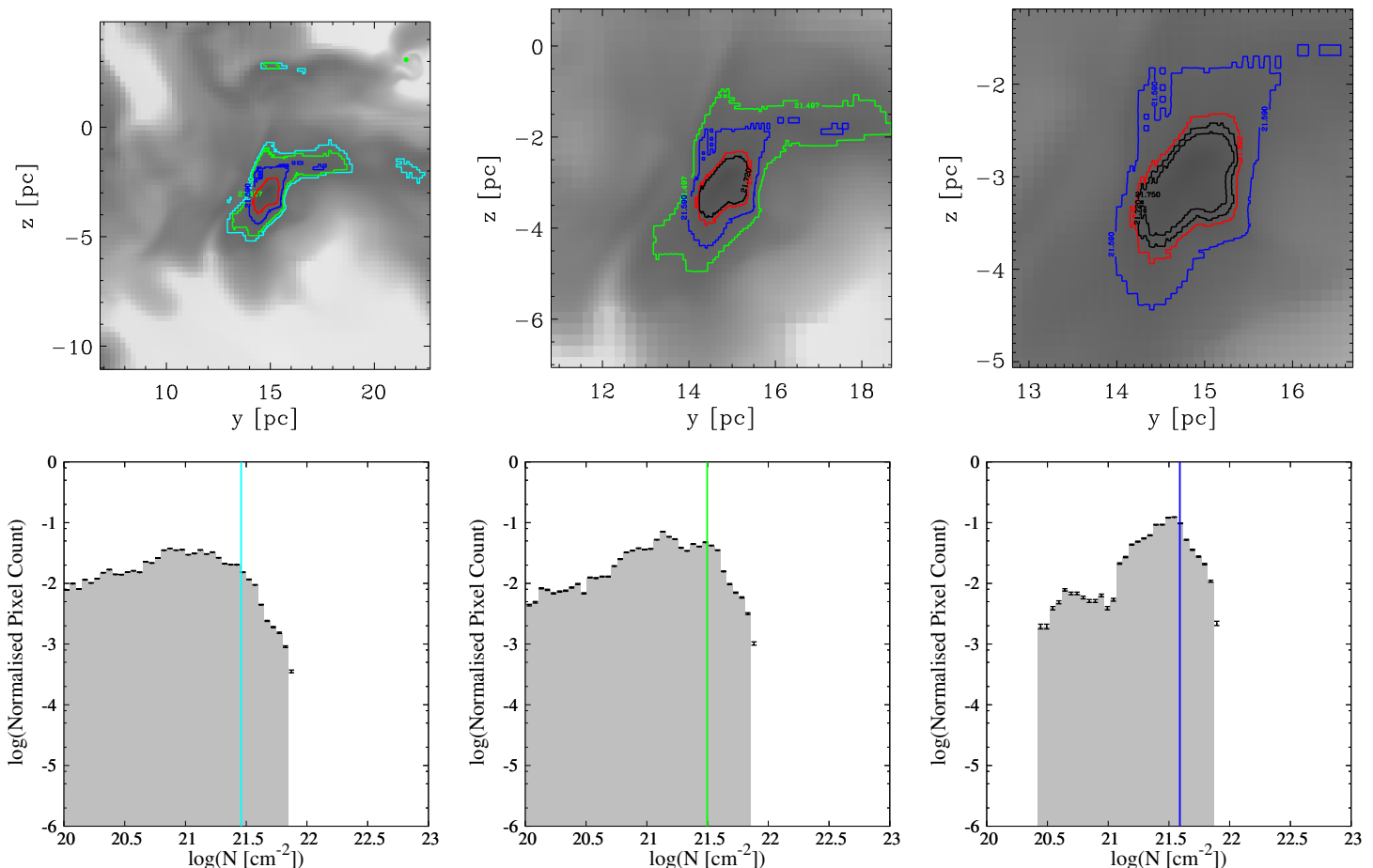


Figure 4. Same as Fig. 3 for a centrally condensed, but non-star-forming region. Please note that the contour spacing for the black contours has changed as the column density profile is rather flat near the center. Note that, in the left panel with a field of view of $16 \times 16 \text{ pc}^2$, turbulent motions in the cloud create regions of enhanced density at various positions within the field of view. This will lead to a last closed contour at higher column densities, if a high density region is located near the boundaries of the field of view.

ning of the power-law tail on towards the maximum column density. However, a sufficiently large field of view captures the log-normal part of the PDF. This was also confirmed by the analysis of the column density distribution of the whole complex. Our results show that the N-PDFs of self-gravitating, turbulent molecular clouds are well described by a log-normal peak and a power-law tail. We conclude that a fully reliable observational study, which takes into account the completeness limit of the PDF must cover a sufficiently large field of view, which might be difficult due to increasing contamination from neighbouring molecular clouds or a decreasing signal-to-noise ratio at the low column-density end of the PDF.

ACKNOWLEDGEMENTS

The authors thank the anonymous referee for their insightful report, which helped to improve the quality of this study. B.K. and R.B. acknowledge funding from the German Science Foundation (DFG) within the Priority Programm "The Physics of the ISM" (SPP 1573) via the grant BA 3706/3-2. R.B. further acknowledges funding for this project from the DFG via the grants BA 3706/4-1, BA 3706/14-1 and BA 3706/15-1. C. F. acknowledges funding provided by the Aus-

tralian Research Council (Discovery Projects DP150104329 and DP170100603, and Future Fellowship FT180100495). B.K. and C.F. acknowledge funding via the Australia-Germany Joint Research Cooperation Scheme (UA-DAAD). C.F. thanks for high-performance computing resources provided by the Leibniz Rechenzentrum and the Gauss Centre for Supercomputing (grants pr32lo, pr48pi and GCS Large-scale project 10391), the Partnership for Advanced Computing in Europe (PRACE grant pr89mu), the Australian National Computational Infrastructure (grant ek9), and the Pawsey Supercomputing Centre with funding from the Australian Government and the Government of Western Australia, in the framework of the National Computational Merit Allocation Scheme and the ANU Allocation Scheme. The simulations were run on HLRN-III under project grand hhp00022. The FLASH code was in part developed by the DOE-supported ASC/Alliance Center for Astrophysical Thermonuclear Flashes at the University of Chicago.

REFERENCES

- Alves J., Lombardi M., Lada C. J., 2017, *A&A*, 606, L2
 Audit E., Hennebelle P., 2005, *A&A*, 433, 1

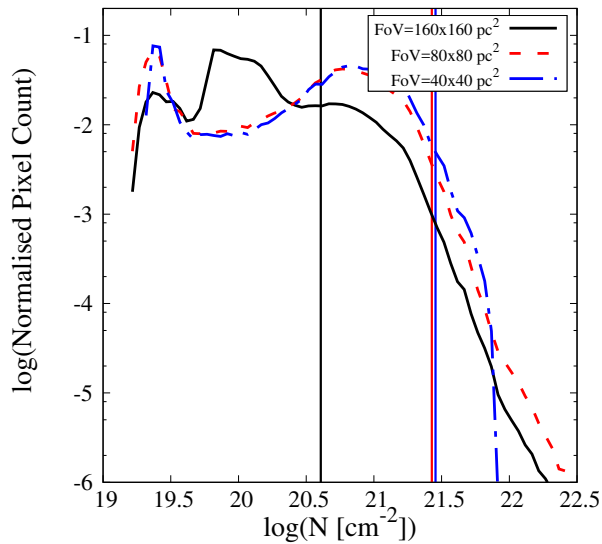


Figure 5. Distribution of column densities for three fields of view centered on the center of the simulation domain. Only the largest field of view contains the whole cloud complex. The smallest field of view also excludes certain star-forming regions. Similar to the individual regions within the complex, the turnover in the distribution is only captured for a sufficiently large FoV.

Ballesteros-Paredes J., Vázquez-Semadeni E., Gazol A., Hartmann L. W., Heitsch F., Colín P., 2011, *MNRAS*, 416, 1436

Banerjee R., Vázquez-Semadeni E., Hennebelle P., Klessen R. S., 2009, *MNRAS*, 398, 1082

Beck R., 2012, *Space Sci. Rev.*, 166, 215

Berger M. J., Colella P., 1989, *Journal of Computational Physics*, 82, 64

Berger M. J., Olinger J., 1984, *Journal of Computational Physics*, 53, 484

Bouchut F., Klingenberg C., Waagan K., 2009, *Numerische Mathematik*

Brunt C. M., 2010, *A&A*, 513, A67

Burkhart B., Lee M.-Y., Murray C. E., Stanimirović S., 2015, *ApJ*, 811, L28

Burkhart B., Stalpes K., Collins D. C., 2017, *ApJ*, 834, L1

Crutcher R. M., Hakobian N., Troland T. H., 2010, *MNRAS*, 402, L64

Elmegreen B. G., Scalo J., 2004, *ARA&A*, 42, 211

Federrath C., Banerjee R., Clark P. C., Klessen R. S., 2010, *ApJ*, 713, 269

Federrath C., Banerjee S., 2015, *MNRAS*, 448, 3297

Federrath C., Klessen R. S., 2012, *ApJ*, 761, 156

Federrath C., Klessen R. S., 2013, *ApJ*, 763, 51

Federrath C., Klessen R. S., Schmidt W., 2008, *ApJ*, 688, L79

Federrath C., Rathborne J. M., Longmore S. N., Kruijssen J. M. D., Bally J., Contreras Y., Crocker R. M., Garay G., Jackson J. M., Testi L., Walsh A. J., 2016, *ApJ*, 832, 143

Federrath C., Roman-Duval J., Klessen R. S., Schmidt W., Mac Low M.-M., 2010, *A&A*, 512, A81

Field G. B., Goldsmith D. W., Habing H. J., 1969, *ApJ*, 155, L149+

Fryxell B., Olson K., Ricker P., Timmes F. X., Zingale M., Lamb D. Q., MacNeice P., Rosner R., Truran J. W., Tufo

H., 2000, *ApJS*, 131, 273

Gazol A., Vázquez-Semadeni E., Kim J., 2005, *ApJ*, 630, 911

Gazol A., Vázquez-Semadeni E., Sánchez-Salcedo F. J., Scalo J., 2001, *ApJ*, 557, L121

Ginsburg A., Federrath C., Darling J., 2013, *ApJ*, 779, 50

Girichidis P., Konstandin L., Whitworth A. P., Klessen R. S., 2014, *ApJ*, 781, 91

Heitsch F., Hartmann L., 2008, *ApJ*, 689, 290

Hennebelle P., Chabrier G., 2011, *ApJ*, 743, L29

Heyer M. H., Brunt C. M., 2004, *ApJ*, 615, L45

Iwasaki K., Inutsuka S.-i., 2014, *ApJ*, 784, 115

Kainulainen J., Beuther H., Henning T., Plume R., 2009, *A&A*, 508, L35

Kainulainen J., Federrath C., Henning T., 2013, *A&A*, 553, L8

Kainulainen J., Federrath C., Henning T., 2014, *Science*, 344, 183

Klessen R. S., Hennebelle P., 2010, *A&A*, 520, A17

Konstandin L., Girichidis P., Federrath C., Klessen R. S., 2012, *ApJ*, 761, 149

Körtgen B., Banerjee R., 2015, *MNRAS*, 451, 3340

Körtgen B., Federrath C., Banerjee R., 2017, *MNRAS*, 472, 2496

Körtgen B., Seifried D., Banerjee R., Vázquez-Semadeni E., Zamora-Avilés M., 2016, *MNRAS*, 459, 3460

Koyama H., Inutsuka S.-i., 2002, *ApJ*, 564, L97

Kritsuk A. G., Norman M. L., Padoan P., Wagner R., 2007, *ApJ*, 665, 416

Kritsuk A. G., Norman M. L., Wagner R., 2011, *ApJ*, 727, L20

Lombardi M., Alves J., Lada C. J., 2015, *A&A*, 576, L1

Lombardi M., Bouy H., Alves J., Lada C. J., 2014, *A&A*, 566, A45

Lukat G., Banerjee R., 2016, *New A*, 45, 14

Nolan C. A., Federrath C., Sutherland R. S., 2015, *MNRAS*, 451, 1380

Ossenkopf V., Mac Low M.-M., 2002, *A&A*, 390, 307

Ossenkopf-Okada V., Csengeri T., Schneider N., Federrath C., Klessen R. S., 2016, *A&A*, 590, A104

Passot T., Vázquez-Semadeni E., 1998, *Phys. Rev. E*, 58, 4501

Pikel’Ner S. B., 1968, *Soviet Ast.*, 11, 737

Schneider N., Bontemps S., Motte F., Ossenkopf V., Klessen R. S., Simon R., Fechtenbaum S., Herpin F., Tremblin P., Csengeri T., Myers P. C., Hill T., Cunningham M., Federrath C., 2016, *A&A*, 587, A74

Schneider N., Csengeri T., Klessen R. S., Tremblin P., Ossenkopf V., Peretto N., Simon R., Bontemps S., Federrath C., 2015, *A&A*, 578, A29

Schneider N., Ossenkopf V., Csengeri T., Klessen R. S., Federrath C., Tremblin P., Girichidis P., Bontemps S., André P., 2015, *A&A*, 575, A79

Tremblin P., Schneider N., Minier V., Didelon P., Hill T., Anderson L. D., Motte F., Zavagno A., André P., Arzoumanian D., Audit E., Benedettini M., Bontemps S., Csengeri T., Di Francesco J., et al., 2014, *A&A*, 564, A106

Truelove J. K., Klein R. I., McKee C. F., Holliman J. H., Howell L. H., Greenough J. A., 1997, *ApJ*, 489, L179+

Vázquez-Semadeni E., 1994, *ApJ*, 423, 681

Vázquez-Semadeni E., Gazol A., Scalo J., 2000, *ApJ*, 540, 271

- Vázquez-Semadeni E., Gómez G. C., Jappsen A., Ballesteros-Paredes J., Klessen R. S., 2009, *ApJ*, 707, 1023
- Vázquez-Semadeni E., Gómez G. C., Jappsen A. K., Ballesteros-Paredes J., González R. F., Klessen R. S., 2007, *ApJ*, 657, 870
- Vázquez-Semadeni E., González-Samaniego A., Colín P., 2017, *MNRAS*, 467, 1313
- Waagan K., Federrath C., Klingenberg C., 2011, *Journal of Computational Physics*, 230, 3331
- Ward R. L., Wadsley J., Sills A., 2014, *MNRAS*, 445, 1575